Cross-Scale Coefficient Selection for Volumetric Medical Image Fusion

Rui Shen, *Student Member, IEEE,* Irene Cheng, *Senior Member, IEEE,* and Anup Basu, *Senior Member, IEEE*

Abstract—Joint analysis of medical data collected from different imaging modalities has become a common clinical practice. Therefore, image fusion techniques, which provide an efficient way of combining and enhancing information, has drawn increasing attention from the medical community. In this paper, we propose a novel cross-scale fusion rule for multiscale decomposition based fusion of volumetric medical images taking into account both intra- and inter-scale consistencies. An optimal set of coefficients from the multiscale representations of the source images is determined by effective exploitation of neighborhood information. An efficient color fusion scheme is also proposed. Experiments demonstrate that our fusion rule generates better results than existing rules.

Index Terms—Medical image fusion, 3D image fusion, fusion rule, multiscale analysis.

I. INTRODUCTION

MEDICAL imaging has become a vital component in routine clinical applications, such as diagnosis and treatment planning [1]. However, because each imaging modality only provides information in a limited domain, many studies prefer joint analysis of imaging data collected from the same patient using different modalities [2]. This requirement of joint analysis led to the introduction of image fusion into the medical field and the development of medical data-oriented fusion techniques [2]–[4]. The goal of image fusion is to provide a single fused image, which provides more accurate and reliable information than any individual source image and in which features may be more distinguishable [5]. Such an enhanced image facilitates visual perception (*e.g.,* by a radiologist) or further image processing (*e.g.,* by a computer-aided detection/diagnosis system, *i.e.,* a CAD system) [5].

Due to its compact and enhanced representation of information, image fusion has been employed in many medical applications. For instance, T_1-weighted (T1W) and T_2-weighted (T2W) magnetic resonance imaging (MRI) scans were fused to segment white matter lesions [6] or cerebral iron deposits [7] and to guide neurosurgical resection of epileptogenic lesions [8]. Computed tomography (CT) and MRI images were fused for neuronavigation in skull base tumor surgery [9]. Fusion of positron emission tomography (PET) and MRI images has proven useful for hepatic metastasis detection [10] and intracranial tumor diagnosis [11]. Single photon emission computed tomography (SPECT) and MRI
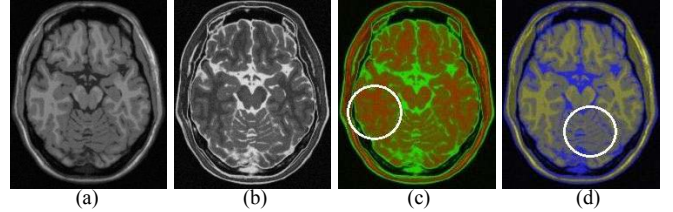

Fig. 1. Overlaying monochrome images using different color channels. Information is transferred from T1W and T2W MRI images into a single image at the cost of reduced image contrast. (a) T1W MRI image; (b) T2W MRI image; (c) Overlaid image using the red and green channels as in [6]; (d) Overlaid image using the yellow and blue channels as in [19].

images were fused for abnormality localization in patients with tinnitus [12]. Multiple fetal cardiac ultrasound scans were fused to reduce imaging artifacts [13]. In addition, the advantages of image fusion over side-by-side analysis of non-fused images have been demonstrated in lesion detection and localization in patients with neuroendocrine tumors [14] and in patients with pretreated brain tumors [15]. Even if image fusion is not performed explicitly, *e.g.,* by a CAD system, it is usually performed subconsciously by radiologists to compare images and better identify abnormalities [16].

A straightforward multi-modal image fusion method is to overlay the source images by manipulating their transparency attributes [17], [18] or by assigning them to different color channels [6], [19]. This overlaying scheme is a fundamental approach in color fusion, a type of image fusion that uses color to expand the amount of information conveyed in a single image [20], but it does not necessarily enhance the image contrast or make image features more distinguishable. An example is given in Figure 1. The overlaying schemes transfer information from two MRI scans into a single image, but at the cost of reduced image contrast (*e.g.,* in the temporal lobe and cerebellum as indicated by the white circles). In this paper, we propose a fusion rule that blends the pixel values in the monochrome source images to combine information while preserving or enhancing contrast. In addition, we show how color fusion can benefit from the monochrome fusion results.

Image fusion can be performed at three different levels, *i.e.,* pixel/data level, feature/attribute level, and symbol/decision level, each of which serves different purposes [5], [20], [21]. Compared with the others, pixel-level fusion directly combines the original information in the source images and is more computationally efficient [21]. According to whether multiscale decomposition (MSD) is used, pixel-level fusion methods can be classified as MSD-based or non-MSD based. Compared to the latter, MSD-based methods have the advantage of ex-

R. Shen, I. Cheng, and A. Basu are with the Department of Computing Science, University of Alberta, Edmonton, AB, T6G 2E8 Canada (e-mail: rshen@ualberta.ca; locheng@ualberta.ca; basu@ualberta.ca).
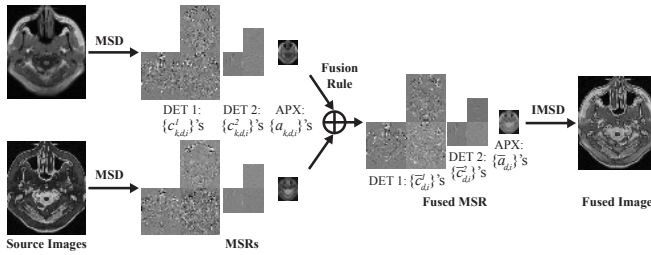
Fig. 2.   General procedure of MSD-based image fusion in a 2D case.

tracting and combining salient features at different scales, and therefore normally produce images with greater information content [20]. The general procedure of MSD-based fusion is illustrated in Figure 2. First, the source images are transformed to multiscale representations (MSRs) using MSD. An MSR is a pyramidal structure with successively reduced spatial resolution; it usually contains one approximation level (APX) storing low-pass coefficients and several detail levels (DETs) storing high-pass or band-pass coefficients. Then, a certain fusion rule is applied to merge coefficients at different scales. Finally, an inverse MSD (IMSD) is applied to the fused MSR to generate the final image.

Two directions can be explored in MSD-based fusion to enhance the fusion quality: advanced MSD schemes and effective fusion rules. Here, we focus on the latter and propose a novel cross-scale (CS) fusion rule, where the belongingness/membership of each fused coefficient to each source image is calculated. Unlike previous methods, our fusion rule calculates an optimal set of coefficients for each scale taking into account large neighborhood information, which guarantees intra- and inter-scale consistencies, i.e., coefficients with similar characteristics are fused in a similar way and artifacts (e.g., aliasing artifacts at object boundaries) are avoided in the results. The effectiveness of this new fusion rule is validated through experiments on 3D medical image fusion. Although it is possible to fuse individual 2D slices in 3D images/volumes separately, the results are not of the same quality as those of 3D fusion due to the lack of between-slice information in the fusion process [22]. Here, therefore, we apply MSD and our CS rule directly to the 3D volumes.

The rest of the paper is organized as follows. Section II reviews previous methods. Section III presents our CS fusion rule and color fusion scheme. Section IV discusses experimental results. Section V gives conclusion and future work.

II. RELATED WORK

A. Multiscale Decomposition

The pyramid transform (PT) and the wavelet transform (WT) are the two categories of MSD schemes that are most commonly employed in image fusion. Among different PT schemes, Laplacian pyramid transform (LPT) [23] is one of the most frequently used. A Laplacian pyramid (LP) is constructed based on its corresponding Gaussian pyramid (GP) by subtracting two adjacent levels. Thus, a DET in the LP encodes the local variations at that scale. The ratio of low-pass pyramid (RoLP) [24] is also constructed based on GP,

but by taking the ratio of two adjacent levels. The gradient pyramid (either explicitly [25] or implicitly [26] constructed) is another type of PT, which is built by applying gradient filters of different orientations to each level of a GP. A standard WT scheme is the discrete WT (DWT) [27], which decomposes a signal into an MSR using scaling (low-pass filtering) and wavelet (high-pass filtering) functions. One drawback of DWT is shift-variance, which tends to cause artifacts along edges in the fused images [28]. Hence, WT schemes that provide shift-invariance, such as dual-tree complex WT (DT-CWT) [29], were also employed in image fusion. Although theoretically the decomposition of an image can be performed iteratively until there is only one coefficient at APX, this will result in serious bias and inaccuracy in the feature selection at low-resolution levels, which impairs the fusion quality [26]. Typically, only a few decomposition levels are therefore used in practice. Please refer to [28], [30] for some analyses on the number of decomposition levels for different MSD schemes.

B. Fusion Rules

In addition to the MSD scheme, the other key factor affecting fusion results is the fusion rule. A fusion rule is the processing that determines the formation of the fused MSR from the MSRs of the source images, and it normally consists of four key components, i.e., activity-level measurement, coefficient grouping, coefficient combination, and consistency verification [5]. In this section, we give a brief review of some representative schemes in these four steps. Please refer to [5], [30] for more detailed discussions and other types of fusion methods (e.g., estimation theory-based method [31]).

1) Activity-Level Measurement: The activity-level measurement reflects the salience of each coefficient in an MSR [28], and it can be categorized into three classes, i.e., coefficient-based activity (CBA), window-based activity (WBA), and region-based activity (RBA) [5]. A CBA measure evaluates each coefficient independently and normally describes the activity level of a coefficient using its absolute value. A WBA measure uses the information within a window to evaluate the coefficient at the window center. A popular choice is the rank filter-based WBA, where the maximum value within a window is normally selected as in [32]. The concept of RBA is similar to WBA except that irregular-shaped regions are used instead of regular-shaped windows. In our CS rule, there is no restriction on the type of activity-level measures to be employed. The focus of our CS rule is to provide a unified framework for the other three key components in a fusion rule, which were usually treated separately in previous methods.

2) Coefficient Grouping: The coefficient grouping schemes can be roughly divided into three categories [5]: no grouping (NG), single-scale grouping (SG), and multiscale grouping (MG). NG means that each coefficient is fused independently; SG means that corresponding coefficients between different subbands at the same scale are fused in the same way; and MG is more restrictive than SG because it also requires that corresponding coefficients between different scales take the same fusion decision. A cross-band SG (CBSG) scheme was proposed in [33], where the same fusion decision for every

set of corresponding detail coefficients at the current scale is made based on the sum of their activity levels and their corresponding coefficients at a higher scale. In [34], an MG scheme was proposed in which the fusion decision for every set of corresponding coefficients across all scales is made based on the weighted average of their activity levels. Our CS rule performs similar to MG, but does not impose such a hard constraint on the fusion decision. Instead, the influence on each coefficient from their corresponding coefficients at adjacent scales is reflected in the membership calculation, and the fusion decision of a coefficient is determined based on its calculated membership.

3) Coefficient Combination: One common coefficient combination scheme for the DETs is the choose-max (CM) strategy, *i.e.,* selecting the coefficient with the highest activity level at each location from the MSRs of the source images as the coefficient at that location in the MSR of the fused image [5]. Two common combination schemes for APX are taking the average (AVG) and taking the weighted average (WA) [25]. In WA, a linear weighting function is applied when the local correlation between corresponding coefficients in a neighborhood in the MSRs of the source images is above a threshold. Our CS rule does not apply combination schemes based directly on coefficient activity levels, but combines coefficients based on their memberships, which results in a more effective scheme utilizing inter- and intra-scale information.

4) Consistency Verification: The consistency verification schemes ensure neighboring coefficients are fused in a similar manner [5]. A majority filter was used in [32] to apply window-based verification (WBV) at each scale. A cross-band verification (CBV) scheme was proposed in [33], where the coefficients at a DET are recalculated if their corresponding coefficients at a lower level do not come from the same MSR. CBV was designed to comply with CBSG. It is also possible that no verification (NV) is applied. Our CS rule does not perform explicit verification, but embeds verification in the coefficient membership calculation process.

C. Medical Image Fusion

The overlaying schemes were discussed in Section I, and here we discuss some activity-level measures and non-MSD-based methods proposed for medical image fusion. Please note that the MSD-based fusion methods discussed in the previous sections can be applied directly to medical image fusion; the DWT+CBA+NG+AVG+CM+NV method, for example, was used in [35] for quality enhancement of real-time 3D echocardiography. A multi-channel pulse coupled neural network was proposed in [36] for 2D medical image fusion. However, the fusion results suffered from loss of local contrast. DWT+WBA+NG+CM+CM+WBV was applied to fuse 2D medical images in [37], where a visibility-based WBA and a local variance-based WBA were proposed for APX and DETs, respectively. In contrast, our focus here is a novel fusion rule rather than a specific activity-level measure.

In [22], a 3D shunting neural network was applied for information decorrelation between source images, and the shunted images were assigned to different color planes. In our method,

a more efficient scheme is proposed, where color fusion of two images is achieved as a natural extension to monochrome fusion. In addition, we emphasize both achromatic and chromatic color contrasts. In [38], the fused 3D medical image was obtained by minimizing a quadratic objective function defined using a gradient-based field. However, that method tends to cause artifacts in smooth image regions due to the form of the objective function. Such artifacts are less likely to appear in our method, where consistencies are emphasized.

III. METHOD

A. Problem Formulation

The source images are assumed to be spatially registered, which is a common assumption in image fusion [5]. Various techniques [1] can be applied to medical image registration. We follow the MSD-based fusion procedure, as illustrated in Figure 2. Let $c_{k,d,i}^n$ and $\bar{c}_{d,i}^n$ denote the i-th coefficients in the d-th subband at the n-th DET of the MSR of the k-th source image and the fused image, respectively, where $n \in [1, N]$. Let $a_{k,d,i}$ and $\bar{a}_{d,i}$ denote the i-th coefficients in the d-th subband at the APX of the MSR of the k-th source image and the fused image, respectively. We assume that a subband at the APX has the same size as a subband at the N-th DET. For PT schemes where the APX is at a higher level, applying an extra step of band-pass filtering can fulfill this assumption. Let $M : \{\bar{c}_{d,i}^n, \bar{a}_{d,i}\} \times \{c_{k,d,i}^n, a_{k,d,i}\} \to [0, 1]$ be a function representing the (partial) membership of $\bar{c}_{d,i}^n$ (or $\bar{a}_{d,i}$) to the MSR of the k-th source image, *i.e.,* the proportion of the contribution from $c_{k,d,i}^n$ (or $a_{k,d,i}$) to $\bar{c}_{d,i}^n$ (or $\bar{a}_{d,i}$) among all corresponding coefficients $\{c_{k,d,i}^n | k = 1, \ldots, K\}$ (or $\{a_{k,d,i} | k = 1, \ldots, K\}$). The memberships can be determined based on local and/or global information in the MSRs. To simplify notation, let $M_{k,d,i}^n$ and $M_{k,d,i}$ denote the coefficient memberships at the n-th DET and the APX, respectively. We have $\sum_k M_{k,d,i}^n = 1$ and $\sum_k M_{k,d,i} = 1$.

For each subband of a DET, where the corresponding coefficients among different MSRs are usually quite distinct from each other, a fused coefficient can be determined as the one with the highest membership:

$$\bar{c}_{d,i}^n = \arg\max_{c_{k,d,i}^n, k:1\ldots K} M_{k,d,i}^n. \tag{1}$$

For the APX, where the corresponding coefficients usually exhibit less diversity compared to those at a DET, a fused coefficient can be determined as a weighted average of all of its corresponding coefficients based on their memberships:

$$\bar{a}_{d,i} = \sum_{k=1}^K M_{k,d,i} a_{k,d,i}. \tag{2}$$

B. Cross-Scale Coefficient Selection

The proposed cross-scale fusion rule aims to pass information within and between each decomposition level to achieve intra- and inter-scale consistencies so that the fused image preserves the most details from the source images while exhibiting minimal artifacts. The basic steps are: 1) pass salient information from a lower level to a higher level in an MSR until APX is reached; 2) calculate the memberships of each

---

Algorithm 1 Basic steps of the LPT+CS fusion scheme.

1: Apply N-level LPT to each source image
2: Apply band-pass filtering to APXs of each source image
3: Compute $\tilde{A}_{k,1,i}^n$'s for DET 1 to N using Equation (3)
4: Compute $M_{k,1,i}$'s at APX using Equations (4) to (6)
5: Compute $M_{k,1,i}^n$'s for DET N to 1 using Equation (7)
6: Select coefficients for fused APX using Equation (2)
7: Select coefficients for fused DETs using Equation (1)
8: Apply inverse LPT to the fused MSR

---

fused coefficient at APX using the passed salient information; 3) use these memberships to guide the coefficient selection at DETs.

Let $A_{k,d,i}^n$ denote the activity level of $c_{k,d,i}^n$. In order to impose inter-scale consistency, the activity levels of coefficients at a lower decomposition level are passed to a higher level as:

$$\tilde{A}_{k,d,i}^n = \begin{cases} \mathrm{erf}(A_{k,d,i}^n), & n = 1; \\ \max(\mathrm{erf}(A_{k,d,i}^n), [\tilde{\mathbf{A}}_{k,d}^{n-1}]_i^{\downarrow 2}), & n \in [2, N], \end{cases} \quad (3)$$

where $\tilde{\mathbf{A}}_{k,d}^n$ denotes the vector containing all $\tilde{A}_{k,d,i}^n$'s in the d-th subband of the MSR of the k-th source image; $[\cdot]^{\downarrow 2}$ denotes downsampling by a factor of 2 in each dimension; and the subscript $[\cdot]_i$ denotes the i-th coefficient. The maximum function is used as a way to ensure inter-scale consistency by allowing the calculation at higher scales to access the most representative salient information at lower scales, which we take as those with high activity levels. $\mathrm{erf} : \mathbb{R} \to [-1, 1]$ is called the Gauss error function, a sigmoid-shaped function. The magnitudes of activity levels of coefficients across different DETs can vary significantly, which makes it difficult to compare the relative importance of salient information across scales. This nonlinear function $\mathrm{erf}(\cdot)$ compresses the activity levels into the same range $[0, 1]$ for non-negative activity levels, which gives a more reasonable comparison of salient information. In addition, it also depresses very high activity levels, which sometimes may be caused by image noise.

At the APX, the passed salient information $\tilde{A}_{k,d,i}^N$'s and the approximation coefficients $a_{k,d,i}$'s are used together to calculate the memberships $M_{k,d,i}$'s. One simple scheme is to directly take normalized $\tilde{A}_{k,d,i}^N$'s as $M_{k,d,i}$'s. However, this scheme does not utilize the visual information embedded in $a_{k,d,i}$'s, which is crucial for producing locally smoothed solutions. The generalized random walks (GRW) proposed in [39] has demonstrated good performance in imposing intra-scale consistency while preserving local details in multi-exposure fusion. Therefore, here we employ GRW to calculate $M_{k,d,i}$'s, which we consider as the steady-state probabilities in the random walks context, by minimizing K similarly-defined energy functions. Let $\mathbf{M}_{k,d}$ denote the vector containing all $M_{k,d,i}$'s, *i.e.,* memberships of all the approximation coefficients in the d-th subband of the fused MSR to the k-th source image. The solution to the k-th energy function is given by:

$$\mathbf{L}_d \mathbf{M}_{k,d} = \tilde{\mathbf{A}}_{k,d}^N. \quad (4)$$

The matrix $\mathbf{L}_d$ encodes the similarities between adjacent coefficients. The entry in the i-th row and j-th column of

$\mathbf{L}_d$ is defined as:

$$\mathbf{L}_{d,ij} = \begin{cases} \sum_{\bar{a}_{d,s} \in \mathcal{N}_{d,i}} W_{d,is} + \sum_k \tilde{A}_{k,d,i}^N, & i = j; \\ -W_{d,ij}, & \bar{a}_{d,j} \in \mathcal{N}_{d,i}; \\ 0, & \text{otherwise,} \end{cases} \quad (5)$$

where $\mathcal{N}_{d,i}$ is the first-order neighborhood of $\bar{a}_{d,i}$. $W_{d,ij}$ represents the expected similarity between $\bar{a}_{d,i}$ and $\bar{a}_{d,j}$ based on the observed approximation coefficients in the MSRs of the source images. $W_{d,ij}$ is defined as follows:

$$W_{d,ij} = \gamma \prod_{k=1}^K \exp\left(-\frac{\|a_{k,d,i} - a_{k,d,j}\|}{\sigma}\right), \quad (6)$$

where γ and σ are weighting factors. Equation (6) assigns a higher penalty to a coefficient pair with greater similarity. Therefore, similar coefficients are more likely to be assigned similar memberships to ensure intra-scale consistency.

Once $M_{k,d,i}$'s are calculated for the APX ($n = N$) using Equations (4) to (6), they are passed down to guide the membership calculation at DETs to impose inter-scale consistency:

$$M_{k,d,i}^n = \begin{cases} M_{k,d,i}, & n = N; \\ \frac{1}{\alpha}[\phi * (\tilde{\mathbf{A}}_{k,d}^n \odot [\mathbf{M}_{k,d}^{n+1}]^{\uparrow 2})]_i, & n \in [1, N-1], \end{cases} \quad (7)$$

where α is a normalization factor rendering $\sum_k M_{k,d,i}^n = 1$; $[\cdot]^{\uparrow 2}$ denotes upsampling by a factor of 2 in each dimension followed by interpolation; $*$ denotes convolution; $\odot$ denotes component-wise multiplication; and ϕ is a low-pass filter that helps to achieve intra-scale consistency. In our current implementation, ϕ is taken as a $5 \times 5 \times 5$ Gaussian filter for each decomposition level of a volume. The filter is constructed using the separable generating kernel in [23] with parameter $a = 0.375^1$. In the following, we give two specific examples of applying our CS rule with two popular MSD schemes, LPT and DWT. However, the concept may be extended to other MSD schemes as well, such as RoLP and DT-CWT.

1) LPT+CS Based Fusion: In order to combine our CS rule with LPT, an extra step of band-pass filtering at the APX is needed to produce a corresponding DET. This DET is only used in the coefficient membership calculation and is not involved in IMSD. Please note that there is only one subband at each decomposition level for LPT. The whole process of LPT+CS-based fusion is summarized in Algorithm 1.

2) DWT+CS Based Fusion: Although it is possible to apply the same scheme for LPT-based fusion to DWT-based fusion, each DET for DWT contains $2^D - 1$ subbands (D is the number of dimensions of the signal), which will result in significantly increased computational cost and poor consistency among subbands. Therefore, corresponding coefficients in different subbands at the same scale are evaluated together and the same membership is assigned to all of them. Hence, $A_{k,d,i}^n$ used in Equation (3) is substituted with the following:

$$\hat{A}_{k,d,i}^n = \max(A_{k,1,i}^n, \dots, A_{k,2^D-1,i}^n). \quad (8)$$

The whole process of DWT+CS-based fusion is summarized in Algorithm 2.

---

[1] This roughly corresponds to a filter generated by a Gaussian kernel with a standard deviation of 1.05.
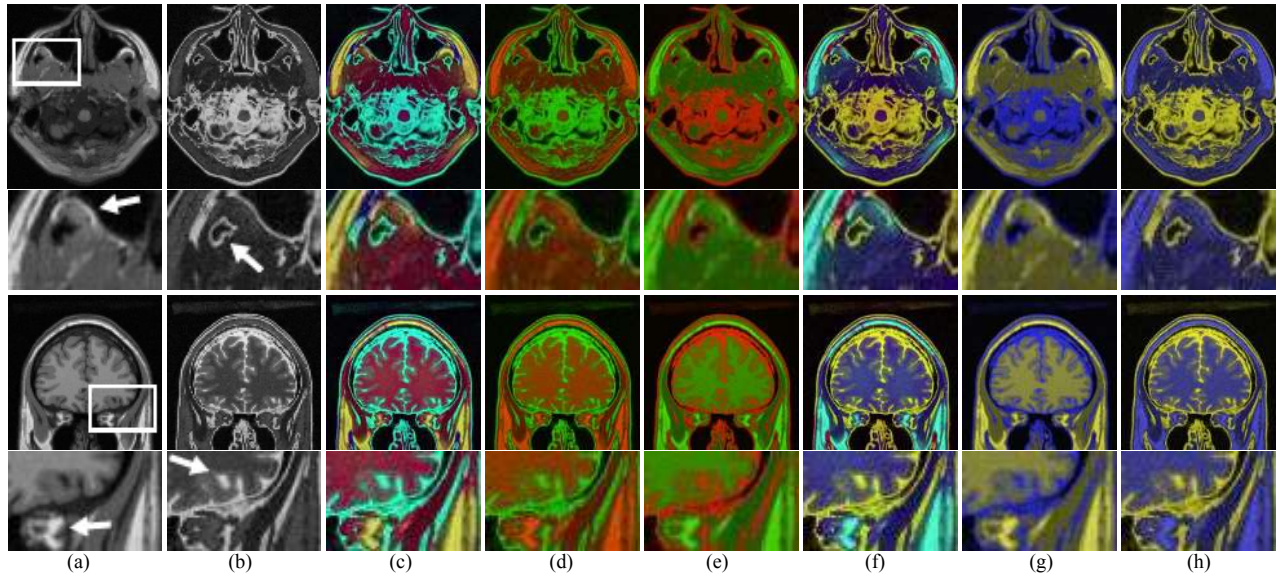
Fig. 3. Comparison between our color fusion scheme and the overlaying scheme. The first row shows a slice along the axial axis from each volume. The second row shows slices along the coronal axis. Our scheme provides more image contrast, which makes the combined details more distinguishable, such as those indicated by the arrows in the insets. (a) T1W MRI slices; (b) T2W MRI slices; (c) Our color fusion results with $\bar{\mathbf{I}}_r^c = \mathbf{I}_1, \bar{\mathbf{I}}_b^c = \mathbf{I}_2$; (d) Overlaid images with $\bar{\mathbf{I}}_r^c = \mathbf{I}_1, \bar{\mathbf{I}}_g^c = \mathbf{I}_2$; (e) Overlaid images with $\bar{\mathbf{I}}_r^c = \mathbf{I}_2, \bar{\mathbf{I}}_g^c = \mathbf{I}_1$; (f) Our color fusion results with $\bar{\mathbf{I}}_r^c = \mathbf{I}_2, \bar{\mathbf{I}}_b^c = \mathbf{I}_1$; (g) Overlaid images with $\bar{\mathbf{I}}_r^c = \bar{\mathbf{I}}_g^c = \mathbf{I}_1, \bar{\mathbf{I}}_b^c = \mathbf{I}_2$; (h) Overlaid images with $\bar{\mathbf{I}}_r^c = \bar{\mathbf{I}}_g^c = \mathbf{I}_2, \bar{\mathbf{I}}_b^c = \mathbf{I}_1$.

Algorithm 2 Basic steps of the DWT+CS fusion scheme.

1: Apply N-level DWT to each source image
2: Compute $\tilde{A}_{k,1,i}^n$'s for DET 1 to N using Equations (8) and (3)
3: Compute $M_{k,1,i}$'s at the APX using Equations (4) to (6)
4: Compute $M_{k,1,i}^n$'s for DET N to 1 using Equation (7)
5: Assign $M_{k,1,i}^n$'s to their corresponding $M_{k,d,i}^n$'s
6: Select coefficients for fused APX using Equation (2)
7: Select coefficients for fused DETs using Equation (1)
8: Apply inverse DWT to the fused MSR

C. Color Fusion

In this section, we introduce an efficient color fusion scheme for the case of two monochrome source images. The color fusion scheme, which utilizes the fusion result from the previous section to further enhance image contrast, is inspired by the color opponency theory in physiology [40], which states that human perception of achromatic and chromatic colors occurs in three independent dimensions, *i.e.,* black-white (luminance), red-green, and yellow-blue. Contrast sensitivity in these three dimensions has been studied by many researchers [41]–[43]. The contrast sensitivity function of luminance shows band-pass characteristics, while the contrast sensitivity functions of both red-green and yellow-blue show low-pass behavior. Therefore, luminance sensitivity is normally higher than chromatic sensitivity except at low spatial frequencies. Hence, the fused monochrome image, which provides combined information and good contrasts, should be assigned to the luminance channel to exploit luminance contrast. In addition, the color-fused image should also provide good contrasts in the red-green and/or yellow-blue channels in order to fully exploit human color perception. To achieve this, we can consider that

red, green, yellow, and blue are arranged on a color circle as in [40], where the red-green axis is orthogonal to the yellow-blue axis and color (actually its hue) transits smoothly from one to another in each quadrant. Then, in order to maximize color contrast/dissimilarity between an object and its local neighborhood in the color-fused image, their hues should come from two opposite quadrants, or at least from two orthogonal hues on the color circle. With these considerations in mind, we have developed the following scheme.

Let $\mathbf{I}_1$ and $\mathbf{I}_2$ denote the two source images and $\bar{\mathbf{I}}$ the monochrome fused image. $\bar{\mathbf{I}}$ is considered as the luminance image of the color-fused image $\bar{\mathbf{I}}^c$. Therefore, if we consider the YUV color space, $\bar{\mathbf{I}}$ is the Y component. Let $\bar{\mathbf{I}}_r^c$, $\bar{\mathbf{I}}_g^c$, and $\bar{\mathbf{I}}_b^c$ denote the red, green, and blue color planes of $\bar{\mathbf{I}}^c$, respectively. The source images are assigned to the red and blue planes in the RGB color space (*i.e.,* $\bar{\mathbf{I}}_r^c = \mathbf{I}_1, \bar{\mathbf{I}}_b^c = \mathbf{I}_2$ or $\bar{\mathbf{I}}_r^c = \mathbf{I}_2, \bar{\mathbf{I}}_b^c = \mathbf{I}_1$), and the green plane is derived by reversing the calculation of the Y component from the RGB color space:

$$\bar{\mathbf{I}}_g^c = (\bar{\mathbf{I}} - 0.299\bar{\mathbf{I}}_r^c - 0.114\bar{\mathbf{I}}_b^c)/0.587. \tag{9}$$

This scheme provides more contrast enhancement than the overlaying schemes, because it fully utilizes color opponency in human perception. Figure 3 provides a visual comparison of slices from two directions. An inset is given below each slice, which clearly shows the improved contrast using our scheme, as indicated by the white arrows (*i.e.,* the sarcolemma in the T1W scan and the mastoid air cells in the T2W scan in the upper row, the orbital apex in the T1W scan and the sulcus in the T2W scan in the lower row). Like in [44], the color characteristics of the color-fused images may be further adjusted according to a user's preference using methods such as color transfer. Researchers [22], [45], [46] have previously studied opponent-color fusion, which is essen-

tially based on opponent processing. After intermediate fused and/or enhanced grayscale images are generated by opponent processing, they are either directly assigned to different color planes (in the case of two source images) or assigned in a way that emphasizes chromatic color contrast (in the case of three or more source images) to form a color-fused image. This is different from our scheme, which aims to maximize both achromatic and chromatic color contrasts in a color-fused image.

IV. EXPERIMENTAL RESULTS AND DISCUSSION

The performance of our cross-scale fusion rule was evaluated on volumetric image fusion of T1W and T2W MRI scans using both synthetic and real data (Section IV-A). After this validation, we demonstrate the capability of our fusion rule to fuse other modalities (Section IV-C). In addition, we have consulted a neurosurgeon and a radiologist. In their opinion, our method not only provides enhanced representations of information, which is useful in applications like diagnosis and neuronavigation, but also offers them the flexibility of combining modalities of their choice, which is important because the data types required are normally application-dependent.

A. Validation of the Proposed Cross-Scale Fusion Rule

In our experiments, only CBA was employed as the activity-level measurement. This is because: 1) as evaluated in [30], CBA is one of the measures that give the best performance; 2) our CS rule places no restriction on the activity level and employing the same activity-level measure in all methods gives a fair comparison between our CS rule and existing fusion rules. Three grouping schemes (NG, CBSG and MG) were considered, as were two combining schemes for APX (AVG and WA). In addition, we considered one combining scheme for DETs (CM) and three verification schemes (NV, WBV, and CBV). Please note that only CM can be used for the APX when MG is used due to the nature of MG and that CBV can only be used with CBSG due to the nature of CBSG. For WA and WBV, we took a $5 \times 5 \times 5$ neighborhood/window. We used the suggested threshold value of 0.85 in WA [25]. The two suggested threshold values of 0.2 and 0.5 in [32] were used in CBV. Two MSD schemes were considered: LPT and DWT. For DWT, we used the wavelet package provided by [47] and employed the 2-band orthogonal near-symmetric filters with $K = 2, L = 6$ [48]. 5-level decomposition was applied in LPT and 4-level decomposition was applied in DWT. Please note that the APX in an N-level LPT has the same size as that in an $(N - 1)$-level DWT. All methods were implemented in Matlab, run on the same computer, and applied directly to the 3D volumes rather than 2D slices. Two free parameters (γ and σ) are in our CS rule. Taking $\gamma = 10, \sigma = 1$ produced the best results in the experiments on the synthetic data; we therefore also used these values in the experiments on real data.

1) Objective Evaluation Metric: The objective metric $Q^{AB/F}$ [49] was employed in evaluating the fusion quality. This metric does not require an ideal composite image, which is difficult to get in practical cases, as a reference image.

$Q^{AB/F}$ has been proven to correspond well with subjective tests among different metrics [50] and is widely used to assess fusion quality [28], [51]. $Q^{AB/F}$ measures the amount of edge information correctly transferred from source images to the fused image; a $Q^{AB/F}$ score is within the range $[0, 1]$, where a higher score indicates a better fusion result.

2) Evaluation Using Synthetic Data: Our CS rule was evaluated on two sets of realistic simulated 3D MRI brain images from BrainWeb [52], which were constructed based on real scans. The scans in each set are spatially registered due to the nature of the simulation. Each scan has $181 \times 217 \times 181$ voxels with 12-bit precision, and the size of each voxel is 1 mm^3. One set contains images of a normal brain, and the other contains images of a brain with moderate multiple sclerosis lesions. The objective evaluation results for LPT- and DWT-based fusion are summarized in Tables I and II (first two rows), respectively. Our CS rule has the best performance in transferring edge information on both datasets, as indicated by the highest $Q^{AB/F}$ scores. LPT performs better than DWT for these datasets. When the other settings are the same, WBV performs better than NV and CBV; and AVG performs better than WA. Therefore, for brevity, only NG+AVG+CM+WBV, CBSG+AVG+CM+WBV, and MG+CM+CM+WBV are visually compared with our CS rule on the lesion dataset in Figure 4. Only one slice along the axial axis from each volume is displayed. These slices are normalized to 8-bit precision only for the purpose of a visual comparison of fusion qualities. Please note that when viewed using a medical image visualization software (*e.g.,* VolView), the voxel values are usually not normalized, but instead, the display range of the voxel values and the image contrast can be interactively adjusted via the window/level setting. The formulation of image fusion as membership calculation, together with the consistency constraints imposed in our CS fusion rule, helps to ensure that associated coefficients are fused similarly in order to avoid fusion artifacts, and to ensure that salient information (*e.g.,* edge information) is correctly transferred from the source images to the fused image. Therefore, compared to other fusion rules, our CS rule not only correctly combined information with high consistency with the source images, but also provided good local contrasts (*e.g.,* between ventricles, grey matter and white matter). As shown in the insets below each slice (refer to the scalp, diploë, grey matter, and white matter indicated by the white arrows), our CS rule successfully eliminated the blocking artifacts shown in MG when coupled with LPT, and it eliminated the aliasing artifacts in NG, CBSG, and MG when coupled with DWT.

3) Evaluation Using Real Data: We also tested our method on fifty real datasets of normal brains randomly selected from the NIH Pediatric MRI Data Repository [53]. Each dataset contains stereotaxically registered MRI scans of the same subject. We used the T1W and T2W scans in each dataset to evaluate the proposed fusion method. Each scan has $197 \times 233 \times 189$ voxels with 32-bit precision, and the size of each voxel is 1 mm^3. The objective evaluation results on five representative datasets for LPT- and DWT-based fusion are summarized in Tables I and II (last five rows), respectively. According to the $Q^{AB/F}$ scores, the fusion rules are ranked

TABLE I
OBJECTIVE EVALUATION RESULTS ON LPT-BASED FUSION OF SYNTHETIC AND REAL DATA USING THE $Q^{AB/F}$ METRIC.

Grouping	CS	NG				CBSG						MG	
APX combining	CS	AVG		WA		AVG			WA			CM	
DET combining	CS	CM		CM		CM			CM			CM	
Verification	CS	NV	WBV	NV	WBV	NV	WBV	CBV	NV	WBV	CBV	NV	WBV
Synthetic normal	**0.7727**	0.6566	0.7022	0.6529	0.6965	0.6532	0.6928	0.5982	0.6492	0.6871	0.5974	0.6609	0.6675
Synthetic lesion	**0.7810**	0.6221	0.6867	0.6120	0.6729	0.6265	0.6853	0.5697	0.6163	0.6718	0.5683	0.6763	0.6837
Real #1002	**0.6662**	0.5661	0.6325	0.5656	0.6321	0.5615	0.6181	0.4758	0.5611	0.6177	0.4755	0.6092	0.6149
Real #1037	0.6301	0.5395	0.5941	0.5399	0.5944	0.54	0.5840	0.4601	0.5404	0.5898	0.4605	0.6243	**0.6305**
Real #1215	**0.6803**	0.5835	0.6521	0.5833	0.6520	0.5783	0.6313	0.4843	0.5781	0.6311	0.4843	0.6169	0.6233
Real #1344	**0.6338**	0.5115	0.5874	0.5103	0.5863	0.5117	0.5726	0.4365	0.5105	0.5714	0.4352	0.5748	0.5807
Real #1372	**0.6560**	0.5627	0.6144	0.5630	0.6147	0.5622	0.6123	0.4765	0.5626	0.6126	0.4771	0.6261	0.6313

TABLE II
OBJECTIVE EVALUATION RESULTS ON DWT-BASED FUSION OF SYNTHETIC AND REAL DATA USING THE $Q^{AB/F}$ METRIC.

| Grouping	CS	NG				CBSG						MG	
APX combining	CS	AVG		WA		AVG			WA			CM	
DET combining	CS	CM		CM		CM			CM			CM	
Verification	CS	NV	WBV	NV	WBV	NV	WBV	CBV	NV	WBV	CBV	NV	WBV
Synthetic normal	**0.7217**	0.5610	0.6719	0.5481	0.6556	0.5579	0.6405	0.4840	0.5443	0.6248	0.4792	0.6115	0.6220
Synthetic lesion	**0.7195**	0.5343	0.6540	0.5133	0.6213	0.5480	0.6217	0.4659	0.5246	0.5898	0.4528	0.6106	0.5834
Real #1002	**0.6140**	0.4950	0.4896	0.4942	0.4887	0.5144	0.5265	0.4110	0.5136	0.5255	0.4110	0.5828	0.5606
Real #1037	0.5578	0.4688	0.4478	0.4690	0.4481	0.4802	0.5180	0.3917	0.4804	0.5183	0.3917	**0.5824**	0.5513
Real #1215	**0.6338**	0.5081	0.5314	0.5073	0.5309	0.5285	0.5508	0.4211	0.5278	0.5502	0.4211	0.5944	0.5740
Real #1344	**0.5638**	0.4347	0.4489	0.4336	0.4475	0.4583	0.5056	0.3765	0.4571	0.5039	0.3761	0.5598	0.5386
Real #1372	0.5908	0.4955	0.4976	0.4959	0.4981	0.5085	0.5722	0.4090	0.5088	0.5730	0.4089	0.5991	**0.6010**
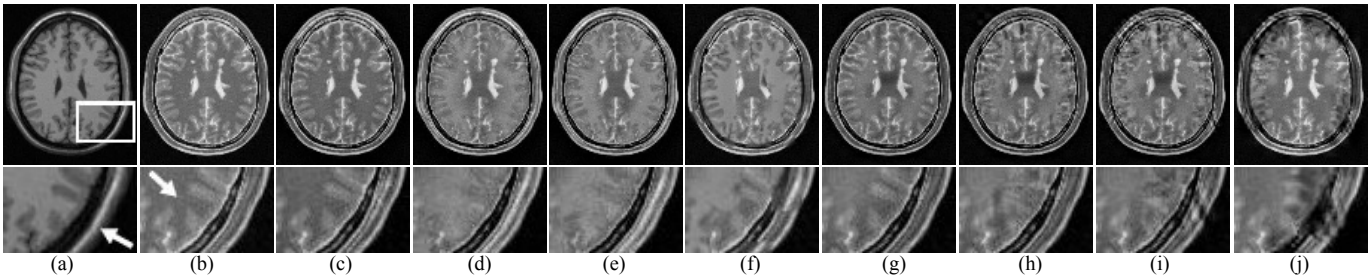
Fig. 4. Comparison of different fusion rules using synthetic MRI brain images. Our CS rule provides better reproduction of local details. (a) T1W MRI image; (b) T2W MRI image; (c) LPT+CS; (d) LPT+NG+AVG+CM+WBV; (e) LPT+CBSG+AVG+CM+WBV; (f) LPT+MG+CM+CM+WBV; (g) DWT+CS; (h) DWT+NG+AVG+CM+WBV; (i) DWT+CBSG+AVG+CM+WBV; (j) DWT+MG+CM+CM+WBV.
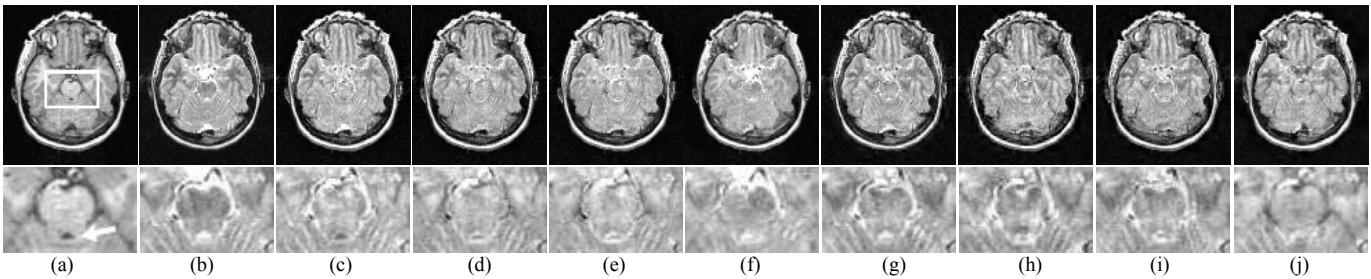

Fig. 5. Comparison of different fusion rules using real dataset #1002. Our CS rule provides better reproduction of local details with better consistencies at region boundaries. (a) T1W MRI image; (b) T2W MRI image; (c) LPT+CS; (d) LPT+NG+AVG+CM+WBV; (e) LPT+CBSG+AVG+CM+WBV; (f) LPT+MG+CM+CM+WBV; (g) DWT+CS; (h) DWT+NG+AVG+CM+WBV; (i) DWT+CBSG+AVG+CM+WBV; (j) DWT+MG+CM+CM+NV.

TABLE III
AVERAGE RANKINGS OF DIFFERENT FUSION RULES ON THE REAL DATA USING THE $Q^{AB/F}$ METRIC.

Grouping	CS	NG				CBSG						MG	
APX combining	CS	AVG		WA		AVG			WA			CM	
DET combining	CS	CM		CM		CM			CM			CM	
Verification	CS	NV	WBV	NV	WBV	NV	WBV	CBV	NV	WBV	CBV	NV	WBV
LPT-based	**1.02**	9.58	4.04	8.58	3.2	10.42	6.18	12.88	9.42	5.36	12.12	4.7	3.5
DWT-based	**1.58**	9.82	9.76	8.98	8.96	7.12	4.84	12.76	6.34	4.16	12.24	1.66	2.78

from 1 (best) to 13 (worst) for each dataset. The average rankings on all the 50 datasets are presented in Table III. Due to the various image conditions in different datasets, a high $Q^{AB/F}$ score in one dataset may be low in a different dataset (*e.g.,* compare the last two rows in Table II). Therefore, in order to give a relatively fair comparison of the average performance of all the 13 fusion rules on the 50 datasets, we used this average ranking method. Our CS rule has the best performance in transferring edge information on the average. With the other settings the same, AVG and WA have very close performance for both LPT and DWT; WBV has better performance than NV and CBV for LPT; NV and WBV have similar performance for DWT+NG; WBV has better performance than NV and CBV for DWT+CBSG; and NV has better performance than WBV for DWT+MG. The results on a representative case (dataset #1002) are visually compared in Figure 5. For brevity, only NG+AVG+CM+WBV, CBSG+AVG+CM+WBV, LPT+MG+CM+CM+WBV, and DWT+MG+CM+CM+NV are visually compared with our CS rule. For the same reason as in Section IV-A2, the slices are normalized to 8-bit precision. As shown in the insets (refer to the cerebellum and the regions around the fourth ventricle as indicated by the white arrow), our CS rule produced better consistencies at region boundaries and gave better local details and contrasts. As Table III reveals, MG+CM+CM+NV performs, on average, at a level close to that of our CS rule in DWT-based fusion, and MG performs slightly better on some datasets as shown in Tables I and II. However, this interpretation is based on the $Q^{AB/F}$ metric, which only considers edge information. Without correctly transferred neighborhood information, the fusion results (even with higher $Q^{AB/F}$ scores) tend to contain artifacts. These artifacts will impair further analysis either by a radiologist or by image processing software. Our CS rule effectively minimizes the occurrence of such artifacts. Figure 6 shows an example. Our CS rule produced better neighborhood consistencies in the white matter.

B. Fusion Quality and the Number of Decomposition Levels

In this experiment, we analyzed the relationship between the fusion quality using our CS rule and the number of decomposition levels (NDL). The seven datasets in Table I were used in this analysis, and we considered four combinations: synthetic+LPT, synthetic+DWT, real+LPT, and real+DWT. For LPT, 3- to 7-level decompositions were considered; for DWT, 2- to 6-level decompositions were considered[2]. To better depict the relationship between fusion quality and NDL, for each MSD scheme on each dataset, we used the $Q^{AB/F}$ score obtained at the lowest NDL as the reference and computed the ratio between the $Q^{AB/F}$ score obtained at a higher NDL and the reference. A ratio larger/less than 1 means an increase/decrease in the score. The average $Q^{AB/F}$ scores at the reference NDL for synthetic+LPT, synthetic+DWT, real+LPT, and real+DWT are 0.7461, 0.6150, 0.6349, and 0.5235, respectively. Figure 7(a) shows the average ratios for each of the four combinations. On the horizontal axis, the size
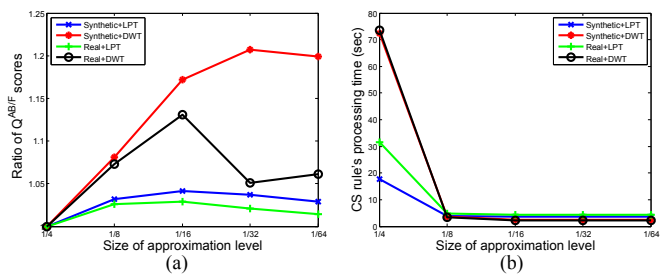

Fig. 7. Analysis of the influence of the number of decomposition levels on the performance of our CS fusion rule. (a) Influence on the $Q^{AB/F}$ scores; (b) Influence on the processing times.

of APX, rather than the NDL, is used to normalize between LPT and DWT. On this axis, $1/M$ means that APX is $1/M$ of the original resolution in each dimension, which corresponds to a $(\log_2 M + 1)$-level LPT or a $(\log_2 M)$-level DWT. The blue line denotes synthetic+LPT, red line synthetic+DWT, green line real+LPT, and black line real+DWT. On average, the highest $Q^{AB/F}$ score is achieved when the APX size is $1/16$, and the performance of our CS rule is less affected by the NDL in LPT than in DWT. The average processing times (in seconds) of our CS rule for each of the four combinations are compared in Figure 7(b). It can be concluded that when the APX size is above $1/8$, there is little improvement on the time performance. The average MSD time of LPT on the seven datasets is about 3 seconds, while DWT takes about 11 seconds. The IMSD time of LPT is about 39% of its MSD time, while the IMSD time of DWT is about 54% of its MSD time. Considering MSD time, fusion time, and IMSD time together, LPT+CS takes only 36% of the time required by DWT+CS on the synthetic datasets, and 45% on the real datasets. From this analysis and the evaluations in Section IV-A, it can be concluded that when combined with the same fusion rule, LPT has better performance than DWT in terms of fusion quality and time performance under our current implementation environment and experimental setup.

C. Application in Fusion of Other Imaging Modalities

Now that the performance of our cross-scale fusion rule has been validated, analyzed, and compared with other fusion rules on T1W/T2W MRI fusion, we further demonstrate its effectiveness in the fusion of other modalities. The registered 3D images used in the experiments in this section are retrieved from [54]. LPT+CS was applied with the same parameter setting as in Section IV-A unless otherwise mentioned.

1) Fusion of CT/MRI: This dataset contains one CT scan and one T1W MRI scan of a patient with cerebral toxoplasmosis. Each scan contains $256 \times 256 \times 24$ voxels with 8-bit precision. Four decomposition levels were applied because the depth of the third dimension is only 24 voxels. As displayed in Figure 8[3], the calcification captured in the CT scan and the soft tissue structures captured in the MRI scan are successfully transferred to the fused image. With our color fusion scheme applied, different features stand out even better.

---

[2]For a very low NDL, a large linear system needs to be solved, which is intractable in practice for 3D medical data; hence, these NDLs were selected.

[3]Some blank pixels at the borders of the displayed images in Figures 8, 9, and 10 were clipped for more concise presentations.
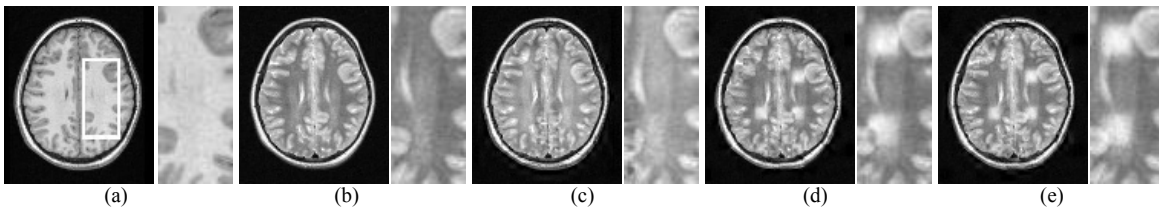
Fig. 6. Comparison of different fusion rules using real dataset #1372. Our CS rule avoids the artifacts produced by the MG rule in the white matter. (a) T1W MRI image; (b) T2W MRI image; (c) DWT+CS; (d) DWT+MG+CM+CM+NV; (e) DWT+MG+CM+CM+WBV.
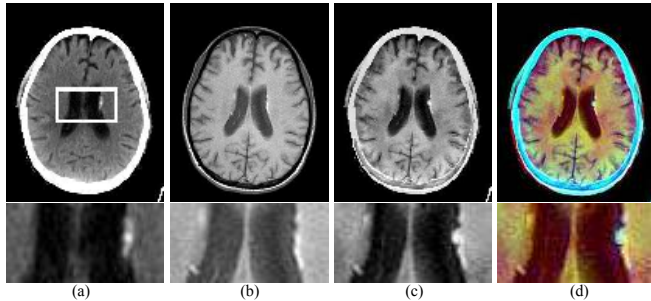

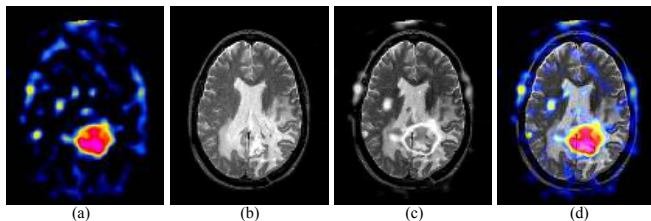Fig. 8. Fusion of CT and T1W MRI images. (a) CT image; (b) T1W MRI image; (c) Fused; (d) Color-fused.

Fig. 9. Fusion of SPECT and T2W MRI images. (a) SPECT image (color-coded); (b) T2W MRI image; (c) Fused; (d) Fused (luminance channel).
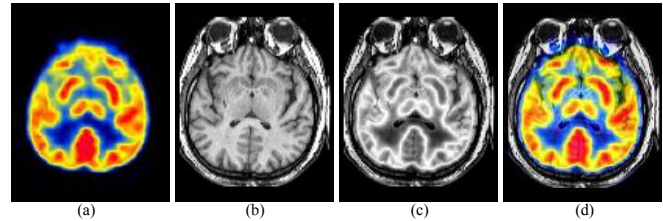

Fig. 10. Fusion of PET and T1W MRI images. (a) PET image (color-coded); (b) T1W MRI image; (c) Fused; (d) Fused (luminance channel).

noising activity-level measure [56] or pre-processing step [39].

V. CONCLUSION AND FUTURE WORK

In this paper, we proposed a cross-scale fusion rule, which selects an optimal set of coefficients for each decomposition level and guarantees intra- and inter-scale consistencies. Experiments on volumetric medical image fusion demonstrated the effectiveness and versatility of our fusion rule, which produced fused images with higher quality than existing rules. An efficient color fusion scheme effectively utilizing monochrome fusion results was also proposed. In future work, we will explore the possibility of extending our technique for 4D medical images. Performing full-scale clinical evaluation catered for individual medical applications is also a valuable future work that will facilitate the adoption of our technique.

2) Fusion of SPECT/MRI: This dataset contains one color-coded SPECT scan and one T2W MRI scan of a patient with anaplastic astrocytoma. Each scan contains $256 \times 256 \times 56$ voxels with 8-bit precision in the luminance channel. When one source image contains color (*e.g.,* the color-coded SPECT scan), a common procedure [55] is to fuse its luminance channel with the other monochrome source image using a monochrome fusion method. As displayed in Figure 9, our method combines the high Thallium uptake shown in the SPECT scan with the anatomical structures shown in the MRI scan in the fused image for better determination of the extent of the tumor, while preserving high image contrast.

3) Fusion of PET/MRI: This dataset contains one color-coded PET scan and one T1W MRI scan of a normal brain. Each scan contains $256 \times 256 \times 127$ voxels with 8-bit precision in the luminance channel. As demonstrated in Figure 10, the metabolic activity revealed in the PET scan and the anatomical structures revealed in the MRI scan are combined in the fused image, providing better spatial relationships.

D. Noise Sensitivity

Noise sensitivity is a common concern for many pixel-level fusion methods [21]. For noisy images, one could employ a de-

REFERENCES

[1] J. B. A. Maintz and M. A. Viergever, "A survey of medical image registration," *Med. Image Anal.*, vol. 2, no. 1, pp. 1–36, 1998.

[2] V. D. Calhoun and T. Adali, "Feature-based fusion of medical imaging data," *IEEE TITB*, vol. 13, no. 5, pp. 711–720, 2009.

[3] B. Solaiman, R. Debon, F. Pipelier, J.-M. Cauvin, and C. Roux, "Information fusion: Application to data and model fusion for ultrasound image segmentation," *IEEE TBME*, vol. 46, no. 10, pp. 1171–1175, 1999.

[4] C. S. Pattichis, M. S. Pattichis, and E. Micheli-Tzanakou, "Medical imaging fusion applications: An overview," in *Proc. 35th Asilomar Conf. Signals, Systems and Computers*, vol. 2, 2001, pp. 1263–1267.

[5] R. S. Blum, Z. Xue, and Z. Zhang, *Multi-Sensor Image Fusion and Its Applications*. CRC Press, 2005, ch. An overview of image fusion, pp. 1–36.

[6] M. C. Valdés Hernández, K. Ferguson, F. Chappell, and J. Wardlaw, "New multispectral MRI data fusion technique for white matter lesion segmentation: method and comparison with thresholding in FLAIR images," *Eur. Radiol.*, vol. 20, no. 7, pp. 1684–1691, 2010.

[7] M. C. Valdés Hernández, T. H. Jeong, C. Murray, M. E. Bastin, F. Chappell, I. J. Deary, and J. Wardlaw, "Reliability of two techniques for assessing cerebral iron deposits with structural magnetic resonance imaging," *J. Magn. Reson. Imaging*, vol. 33, no. 1, pp. 54–61, 2011.

[8] M. Mahvash, R. König, H. Urbach, J. von Ortzen, B. Meyer, J. Schramm, and C. Schaller, "FLAIR-/T1-/T2-co-registration for image-guided diagnostic and resective epilepsy surgery," *Neurosurgery*, vol. 58, no. 1, pp. 69–75, 2006.

[9] S. F. Nemec, M. A. Donat, S. Mehrain, K. Friedrich, C. Krestan, C. Matula, H. Imhof, and C. Czerny, "CT-MR image data fusion for computer assisted navigated neurosurgery of temporal bone tumors," *Eur. J. Radiol.*, vol. 62, no. 2, pp. 192–198, 2007.

[10] O. F. Donati, T. F. Hany, C. S. R. CS, G. K. von Schulthess, B. Marincek, B. Seifert, and D. Weishaupt, "Value of retrospective fusion of PET and MR images in detection of hepatic metastases: Comparison with ^{18}F-FDG PET/CT and Gd-EOB-DTPA-enhanced MRI," *J. Nucl. Med.*, vol. 51, no. 5, pp. 692–699, 2010.

[11] A. Boss, S. Bisdas, A. Kolb, M. Hofmann, U. Ernemann, C. D. Claussen, C. Pfannenberg, B. J. Pichler, M. Reimold, and L. Stegger, "Hybrid PET/MRI of intracranial masses: Initial experiences and comparison to PET/CT," *J. Nucl. Med.*, vol. 51, no. 8, pp. 1198–1205, 2010.

[12] M. Farhadi, S. Mahmoudian, F. Saddadi, A. R. Karimian, M. Mirzaee, M. Ahmadizadeh, K. Ghasemikian, S. Gholami, E. Ghoreyshi, S. Beyty, A. Shamshiri, S. Madani, V. Bakaev, S. Moradkhani, and G. Raeisali, "Functional brain abnormalities localized in 55 chronic tinnitus patients: Fusion of SPECT coincidence imaging and MRI," *J. Cereb. Blood. Flow. Metab.*, vol. 30, no. 4, p. 864870, 2010.

[13] M. J. Gooding, K. Rajpoot, S. Mitchell, P. Chamberlain, S. H. Kennedy, and J. A. Noble, "Investigation into the fusion of multiple 4-D fetal echocardiography images to improve image quality," *Ultrasound Med. Biol.*, vol. 36, no. 6, pp. 957–966, 2010.

[14] H. Amthauer, T. Denecke, T. Rohlfing, J. Ruf, M. Bohmig, M. Gutberlet, U. Plokinger, R. Felix, and A. J. Lemke, "Value of image fusion using single photon emission computed tomography with integrated low dose computed tomography in comparison with a retrospective voxel-based method in neuroendocrine tumours," *Eur. Radiol.*, vol. 15, no. 7, pp. 1456–1462, 2005.

[15] H. Amthauer, R. Wurm, D. Kuczer, J. Ruf, R. Michel, J. Eisenacher, F. Stockhammer, T. Denecke, R. Felix, and M. Plotkin, "Relevance of image fusion with MRI for the interpretation of I-123 iodo-methyl-tyrosine scans in patients with suspected recurrent or residual brain tumor," *Clin. Nucl. Med.*, vol. 31, no. 4, pp. 189–192, 2006.

[16] A. Jackson, N. A. Thacker, and S. M. Stivaros, *Image Processing in Radiology: Current Applications*. Springer, 2007, ch. 3D image fusion, pp. 101–122.

[17] T. Z. Wong, T. G. Turkington, T. C. Hawk, and R. E. Coleman, "PET and brain tumor image fusion," *Cancer J.*, vol. 10, no. 4, pp. 234–242, 2004.

[18] F. L. Giesel, A. Mehndiratta, J. Locklin, M. J. McAuliffe, S. White, P. L. Choyke, M. V. Knopp, B. J. Wood, U. Haberkorn, and H. von Tengg-Kobligk, "Image fusion using CT, MRI and PET for treatment planning, navigation and follow up in percutaneous RFA," *Exp. Oncol.*, vol. 31, no. 2, pp. 106–114, 2009.

[19] B. C. Porter, D. J. Rubens, J. G. Strang, J. Smith, S. Totterman, and K. J. Parker, "Three-dimensional registration and fusion of ultrasound and MRI using major vessels as fiducial markers," *IEEE Trans. Med. Imag.*, vol. 20, no. 4, pp. 354–359, 2001.

[20] M. I. Smith and J. P. Heather, "A review of image fusion technology in 2005," in *Proc. SPIE*, vol. 5782, 2005, pp. 29–45.

[21] G. Piella, "A general framework for multiresolution image fusion: from pixels to regions," *Inf. Fusion*, vol. 4, no. 4, pp. 259–280, 2003.

[22] M. Aguilar and J. R. New, "Fusion of multi-modality volumetric medical imagery," in *Proc. Int. Conf. Inf. Fusion*, vol. 2, 2002, pp. 1206–1212.

[23] P. Burt and E. H. Adelson, "The Laplacian pyramid as a compact image code," *IEEE Trans. Comm.*, vol. 31, no. 4, pp. 532–540, 1983.

[24] A. Toet, "Hierarchical image fusion," *Mach. Vision Appl.*, vol. 3, no. 1, pp. 1–11, 1990.

[25] P. J. Burt and R. J. Kolczynski, "Enhanced image capture through fusion," in *Proc. ICCV*, 1993, pp. 173–182.

[26] V. Petrović and C. Xydeas, "Gradient-based multiresolution image fusion," *IEEE TIP*, vol. 13, no. 2, pp. 228–237, 2004.

[27] S. G. Mallat, "A theory for multiresolution signal decomposition: The wavelet representation," *IEEE TPAMI*, vol. 11, no. 7, pp. 674–693, 1989.

[28] S. Li, B. Yang, and J. Hu, "Performance comparison of different multi-resolution transforms for image fusion," *Inf. Fusion*, vol. 12, no. 2, pp. 74–84, 2011.

[29] I. W. Selesnick, R. G. Baraniuk, and N. C. Kingsbury, "The dual-tree complex wavelet transform," *IEEE Signal Process. Magazine*, vol. 22, no. 6, pp. 123–151, 2005.

[30] G. Pajares and J. M. de la Cruz, "A wavelet-based image fusion tutorial," *Pattern Recognit.*, vol. 37, no. 9, pp. 1855–1872, 2004.

[31] J. Yang and R. S. Blum, "Image fusion using the expectation-maximization algorithm and a hidden Markov model," in *Proc. 60th IEEE Veh. Tech. Conf.*, vol. 6, 2004, pp. 4563–4567.

[32] H. Li, B. S. Manjunath, and S. K. Mitra, "Multisensor image fusion using the wavelet transform," *Graph. Models Image Process.*, vol. 57, no. 3, pp. 235–245, 1995.

[33] V. Petrović and C. Xydeas, "Cross-band pixel selection in multiresolution image fusion," in *Proc. SPIE*, vol. 3719, 1999, pp. 319–326.

[34] Z. Zhang and R. S. Blum, "Region-based image fusion scheme for concealed weapon detection," in *Proc. Ann. Conf. Inf. Sciences and Systems*, 1997, pp. 168–173.

[35] K. Rajpoot, J. A. Noble, V. Grau, C. Szmigielski, and H. Becher, "Multiview RT3D echocardiography image fusion," in *Proc. FIMH*, vol. 5528, 2009, pp. 134–143.

[36] Z. Wang and Y. Ma, "Medical image fusion using m-PCNN," *Inf. Fusion*, vol. 9, no. 2, pp. 176–185, 2008.

[37] Y. Yang, D. S. Park, S. Huang, and N. Rao, "Medical image fusion via an effective wavelet-based approach," *EURASIP J. Advances in Signal Process.*, vol. 2010, no. 579341, pp. 1–13, 2010.

[38] C. Wang and Z. Ye, "First-order fusion of volumetric medical imagery," *IEE Proc., Vis. Image Process.*, vol. 153, no. 2, pp. 191–198, 2006.

[39] R. Shen, I. Cheng, J. Shi, and A. Basu, "Generalized random walks for fusion of multi-exposure images," *IEEE TIP*, vol. 20, no. 12, pp. 3634–3646, 2011.

[40] E. Hering, *Outlines of a Theory of the Light Sense*. Harvard University Press, 1964, ch. The natural color system, pp. 25–65.

[41] K. T. Mullen, "The contrast sensitivity of human colour vision to red-green and blue-yellow chromatic gratings," *J. Physiol.*, vol. 359, pp. 381–400, 1985.

[42] J. M. Rovamo, M. I. Kankaanpaa, and H. Kukkonen, "Modelling spatial contrast sensitivity functions for chromatic and luminance-modulated gratings," *Vision Res.*, vol. 39, no. 14, pp. 2387–2398, 1999.

[43] J. E. Thornton and E. N. Pugh, "Red/green color opponency at detection threshold," *Science*, vol. 219, no. 4581, pp. 191–193, 1983.

[44] A. Toet, "Natural colour mapping for multiband nightvision imagery," *Inf. Fusion*, vol. 4, no. 3, pp. 155–166, 2003.

[45] A. M. Waxman, M. Aguilar, D. A. Fray, D. B. Ireland, J. P. Racamato Jr., W. D. Ross, J. E. Carrick, A. N. Gove, M. C. Seibert, E. D. Savoye, R. K. Reich, B. E. Burke, W. H. McGonagle, and D. M. Craig, "Solid-state color night vision: Fusion of low-light visible and thermal infrared imagery," *Linc. Lab. J.*, vol. 11, no. 1, pp. 41–60, 1998.

[46] M. Aguilar, D. A. Fay, W. D. Ross, A. M. Waxman, D. B. Ireland, and J. P. Racamato, "Real-time fusion of low-light CCD and uncooled IR imagery for color night vision," in *Proc. SPIE*, vol. 3364, 1998, pp. 124–135.

[47] S. Cai, K. Li, and I. Selesnick, "Wavelet software at Polytechnic University, Brooklyn, NY," http://eeweb.poly.edu/iselesni/WaveletSoftware/.

[48] A. F. Abdelnour and I. W. Selesnick, "Design of 2-band orthogonal near-symmetric CQF," in *Proc. IEEE ICASSP*, vol. 6, 2001, pp. 3693–3696.

[49] C. S. Xydeas and V. Petrović, "Objective image fusion performance measure," *Electron. Lett.*, vol. 36, no. 4, pp. 308–309, 2000.

[50] V. Petrović, "Subjective tests for image fusion evaluation and objective metric validation," *Inf. Fusion*, vol. 8, no. 2, pp. 208–216, 2007.

[51] Z. Liu, E. Blasch, Z. Xue, J. Zhao, R. Laganiere, and W. Wu, "Objective assessment of multiresolution fusion algorithms for context enhancement in night vision: A comparative study," *IEEE TPAMI*, vol. 34, no. 1, pp. 94–109, 2011.

[52] R. K.-S. Kwan, A. C. Evans, and G. B. Pike, "MRI simulation-based evaluation of image-processing and classification methods," *IEEE Trans. Med. Imag.*, vol. 18, no. 11, pp. 1085–1097, 1999, http://www.bic.mni.mcgill.ca/brainweb/.

[53] Brain Development Cooperative Group and A. C. Evans, "The NIH MRI study of normal brain development," *NeuroImage*, vol. 30, no. 1, pp. 184–202, 2006, https://nihpd.crbs.ucsd.edu/nihpd/info/.

[54] K. A. Johnson and J. A. Becker, "The whole brain altas," http://www.med.harvard.edu/aanlib/.

[55] Z. Xue and R. S. Blum, "Concealed weapon detection using color image fusion," in *Proc. Int. Conf. Inf. Fusion*, vol. 1, 2003, pp. 622–627.

[56] A. Loza, D. Bull, N. Canagarajah, and A. Achim, "Non-Gaussian model-based fusion of noisy images in the wavelet domain," *Comput. Vis. Image Und.*, vol. 114, no. 1, pp. 54–65, 2010.